Electronic and optical properties of III-V and II-VI semiconductor superlattices

N. F. Johnson, H. Ehrenreich,* P. M. Hui, and P. M. Young
Division of Applied Sciences, Harvard University, Cambridge, Massachusetts 02138
(Received 11 July 1989)

The electronic structure and optical properties of III-V and II-VI semiconductor superlattices are treated theoretically using a superlattice-representation formalism. The band structure is obtained from superlattice $\mathbf{K}\cdot\mathbf{p}$ theory. The theory is based on closed analytic calculations of the superlattice states at wave vector $\mathbf{K}=\mathbf{0}$ and the envelope-function approach. The known parameters of the bulk constituents represent the only input. The electron effective masses and gaps of $GaAs/Ga_{1-x}Al_xAs$ (type I), InAs/GaSb (type II), and HgTe/CdTe (type III) are investigated for a wide range of layer widths using the recently deduced large valence-band offset of HgTe/CdTe. The behavior of the masses is also discussed in terms of the f-sum rule. The calculated fundamental absorption coefficients for InAs/GaSb and HgTe/CdTe are in excellent agreement with experimental data. The intersubband absorption between the lowest two superlattice conduction bands is investigated. In the thick-barrier limit of $GaAs/Ga_{1-x}Al_xAs$ the absorption can be larger than the fundamental absorption and as narrow as a laser linewidth. In the thin-barrier limit the absorption is smaller and broader, as illustrated for $In_xGa_{1-x}As/In_yAl_{1-y}As$.

I. INTRODUCTION

This paper presents a detailed treatment of the electronic structure and optical properties of III-V and II-VI semiconductor superlattices (SL's) based on and extending previous brief publications.[1-3] The present theoretical approach describes the superlattice as a perfectly periodic system within the envelope-function approximation.[4,5] The standard formalism for bulk periodic solids, including $\mathbf{K}\cdot\mathbf{p}$ theory, is then directly applicable. The only input parameters for the theory are those of the bulk materials involved in the superlattice. This approach has previously been used (i) to extend the well-known bulk f-sum rule to superlattices,[1] (ii) to predict large intersubband optical absorption between the lowest two superlattice conduction bands,[2] and (iii) to propose a resolution of the valence-band offset controversy in HgTe/CdTe SL's.[3] The results presented in this paper exhibit the excellent agreement obtained between the experimental values of quantities such as the fundamental absorption coefficients for InAs/GaSb and $HgTe/Hg_{1-x}Cd_xTe$ and the results obtained using this theoretical approach.

The present approach, described in Sec. II, is easy to implement without large scale computation and yields reliable results for superlattice properties (e.g., effective masses) both perpendicular and parallel to the planes in the energy region of interest. The superlattice states at superlattice wave vector $\mathbf{K}=\mathbf{0}$ are first expressed in terms of known bulk $\mathbf{k}\cdot\mathbf{p}$ parameters using the envelope-function approach and a modified bulk Kane model as input. The adequacy of this limited-basis $\mathbf{k}\cdot\mathbf{p}$ model has recently been verified by comparison with the state-of-the-art extended-basis model of McGill and co-workers.[6] The $\mathbf{K}=\mathbf{0}$ masses can then be obtained analytically using the f-sum rule.[1] Superlattice $\mathbf{K}\cdot\mathbf{p}$ theory is employed to yield the SL band structure at finite $\mathbf{K}$. The optical properties are then obtained from knowledge of the finite $\mathbf{K}$ electronic properties.

Sections III and IV present a quantitative comparison of the electronic and optical properties of several technologically important SL's. Section III A describes the layer width dependencies of the SL electron mass and gap in $GaAs/Ga_{1-x}Al_xAs$ (type I), InAs/GaSb (type II), and HgTe/CdTe (type III). The behavior of the masses is then discussed in terms of the f-sum rule for the InAs/GaSb SL (Sec. III B), which is of theoretical interest because the electron and hole wave functions are concentrated in separate layers. Section III C compares the band structures of the three SL's.

The discussion of optical properties in Sec. IV is essentially self-contained. The primary motivation for studying HgTe/CdTe, and to a lesser extent InAs/GaSb, is for use in infrared detectors. This application makes use of *fundamental* SL absorption in the 10-μm range. The present theory yields fundamental absorption coefficients in excellent agreement with experimental data[7,8] for both $HgTe/Hg_{1-x}Cd_xTe$ and InAs/GaSb (Sec. IV A). The type-I SL's considered here have been recently proposed for use in optoelectronics owing to the large *intersubband* oscillator strength between the lowest two SL conduction bands, $C1$ and $C2$.[2,9-12] In particular, the $C1\rightarrow C2$ absorption in $GaAs/Ga_{1-x}Al_xAs$ with thick $Ga_{1-x}Al_xAs$ barriers has been suggested for use in carrier-activated light modulation in the 10-μm range.[2] The corresponding absorption coefficient is shown here to be sharply peaked with magnitude $\sim 10^4$ cm^{-1} (Sec. IV B). In the thin-barrier SL limit the absorption coefficient is predicted to be broader and smaller ($\sim 10^3$ cm^{-1}), as illustrated in Sec. IV B for $In_xGa_{1-x}As/In_yAl_{1-y}As$.

II. FORMALISM

The Hamiltonian in an A/B superlattice is given by

$$H(\mathbf{r})=\frac{p^2}{2m}+V(\mathbf{r})+\frac{\hbar}{4m^2c^2}[\sigma\times\nabla V(\mathbf{r})]\cdot\mathbf{p} \qquad (1)$$

where $V(\mathbf{r})$ is the microscopic SL potential, $\mathbf{p}$ is the momentum operator, and the last term describes the spin-orbit coupling. The SL wave function at SL wave vector $\mathbf{K}$ in band L satisfies

$$H(\mathbf{r})\langle \mathbf{r}|L\mathbf{K}\rangle = E_L(\mathbf{K})\langle \mathbf{r}|L\mathbf{K}\rangle \tag{2}$$

where $E_L(\mathbf{K})$ is the corresponding energy. The z (or $\perp$) axis is chosen as the SL growth direction with $z=0$ defined as the center of a given layer of material A. For lattice-matched SL's having the xy interface plane coincident with a crystal plane, $\mathbf{K}=(k_x,k_y,K_\perp)\equiv(\mathbf{K}_\parallel,K_\perp)$ where k_x and k_y are bulk wave vectors.

We employ the envelope-function approach[5] to express SL quantities in terms of bulk electronic structure parameters. The envelope-function expansion is given by

$$\langle \mathbf{r}|L\mathbf{K}\rangle = \sum_n F_n(L,\mathbf{K};\mathbf{r})\langle \mathbf{r}|n0\rangle \tag{3}$$

where $\langle \mathbf{r}|n0\rangle$ is the bulk Bloch function for band n at $\mathbf{k}=0$ in either material A or B and $F_n(L,\mathbf{K};\mathbf{r})$ is the envelope function. For the well-lattice-matched SL's considered here, $\langle \mathbf{r}|n0\rangle$ may be assumed to be the same in A and B. This assumption is justified here by the similarity of the bulk pseudopotentials and momentum-matrix elements for the A and B bulk materials under consideration.[5,13] The envelope function $F_n(L,\mathbf{K};\mathbf{r})$ is taken to be slowly varying on the scale of the bulk unit-cell size, and can therefore be cell averaged. This approximation together with the substitution of Eq. (3) into Eq. (1) yields a multiband effective-mass-like Hamiltonian

$$H^{k\cdot p}_{A(B)}(k_x,k_y,k_z\rightarrow -i(\partial/\partial z))\mathbf{F}(L,\mathbf{K};\mathbf{r}) = E_L(\mathbf{K})\mathbf{F}(L,\mathbf{K};\mathbf{r}) \tag{4}$$

governing the envelope functions at $\mathbf{r}$ in a layer of material A (B). The matrix $H^{k\cdot p}_{A(B)}(\mathbf{k})$ is the general $\mathbf{k}\cdot\mathbf{p}$ matrix for bulk A (B) material and $\mathbf{F}(L,\mathbf{K};\mathbf{r})$ is a column vector with components $F_n(L,\mathbf{K};\mathbf{r})$. The boundary conditions for $\mathbf{F}(L,\mathbf{K};\mathbf{r})$, to be specified explicitly later, are obtained by integrating Eq. (4) across an interface, and are consistent with continuity of the cell-averaged current.[14] The bulk momentum-matrix elements of $H^{k\cdot p}_{A(B)}(\mathbf{k})$ contain the effects of the rapidly varying $\langle \mathbf{r}|n0\rangle$'s.

The envelope-function equation [Eq. (4)] is truncated here to a limited number of bulk bands by using the specific form of $H^{k\cdot p}_{A(B)}(\mathbf{k})$ corresponding to the modified Kane model[13] including finite-spin-orbit splitting.[15] A finite bulk heavy-hole mass is obtained though inclusion of remote band effects via perturbation theory. The eight bulk $\mathbf{k}=0$ basis states $\langle r|n0\rangle$ being considered are defined in Table I in terms of the states $|S\rangle$, $|X\rangle$, $|Y\rangle$, and $|Z\rangle$ using the notation of Ref. 13. The corresponding $\mathbf{k}=0$ energies $E_n(0)$ in material A are also given. Each $\langle \mathbf{r}|n0\rangle$ can be characterized by $|J,M_J\rangle$ as shown in Table I, where M_J is the z component of the total angular momentum J.[13]

The SL states at $\mathbf{K}=(0,0,K_\perp)$ can be labeled by M_J which remains a good quantum number.[5] Specifically $M_J=\pm\frac{1}{2}$ for the light particle SL states, and $M_J=\pm\frac{3}{2}$ for the heavy-hole SL states. The resulting 8×8 matrix equation obtained from Eq. (4) at $\mathbf{K}=(0,0,K_\perp)$ consists of two equivalent 4×4 blocks corresponding to positive and negative M_J values, respectively. Table II shows the 4×4 block corresponding to positive M_J (i.e., $M_J=+\frac{1}{2}$ and $+\frac{3}{2}$). The 4×4 block corresponding to negative M_J can be obtained from Table II by replacing F_1 by F_2, F_3 by F_4, F_5 by F_6, and F_7 by F_8. Each F_n is independent of x and y. The Kane-matrix element $P=-i\sqrt{2/3}\langle S|p_z|Z\rangle$ which appears in Table II is deduced from experimental bulk masses and gaps. The function $m^{\mathrm{HH}}(z)$ corresponds to the bulk heavy-hole mass $m^{\mathrm{HH}}_{A(B)}$ when z is in material A or B, respectively. The quantities $V_{\Gamma_6}(z)$, $V_{\Gamma_7}(z)$, and $V_{\Gamma_8}(z)$ are set equal to zero in material A. They are given in material B by the differences V_{Γ_6}, V_{Γ_7}, and V_{Γ_8} between the corresponding bulk band edges of material A and B as shown in Fig. 1. The quantities $m^{\mathrm{HH}}(z)$, $V_{\Gamma_6}(z)$, $V_{\Gamma_7}(z)$, and $V_{\Gamma_8}(z)$ are assumed to change abruptly at an interface on the macroscopic length scale of the SL period.

The coupled differential equations for $F_n(L,K_\perp;z)$ in Table II can be rewritten equivalently as

TABLE I. Bulk modified Kane model $\mathbf{k}=0$ states $|n0\rangle$, energies $E_n(0)$ in material A, and angular momentum labels $|J,M_J\rangle$ for Γ_6, Γ_7, and Γ_8 bulk band edges, using the notation of Refs. 5 and 13. The origin of energy is defined as the Γ_6 edge. The bulk band gap and spin-orbit splitting in bulk A material are E_A and Δ_A, respectively.

	$n:\|n0\rangle$	$E_n(0)$	$\|J,M_J\rangle$
Γ_6	$1:\|S\uparrow\rangle$	0	$\|\frac{1}{2},+\frac{1}{2}\rangle$
	$2:\|S\downarrow\rangle$	0	$\|\frac{1}{2},-\frac{1}{2}\rangle$
Γ_8	$3:\sqrt{2/3}\|Z\uparrow\rangle-\sqrt{1/6}\|X+iY\downarrow\rangle$	$-E_A$	$\|\frac{3}{2},+\frac{1}{2}\rangle$
	$4:\sqrt{2/3}\|Z\downarrow\rangle+\sqrt{1/6}\|X-iY\uparrow\rangle$	$-E_A$	$\|\frac{3}{2},-\frac{1}{2}\rangle$
	$5:\sqrt{1/2}\|X+iY\uparrow\rangle$	$-E_A$	$\|\frac{3}{2},+\frac{3}{2}\rangle$
	$6:\sqrt{1/2}\|X-iY\downarrow\rangle$	$-E_A$	$\|\frac{3}{2},-\frac{3}{2}\rangle$
Γ_7	$7:\sqrt{1/3}\|Z\uparrow\rangle+\sqrt{1/3}\|X+iY\downarrow\rangle$	$-E_A-\Delta_A$	$\|\frac{1}{2},+\frac{1}{2}\rangle$
	$8:\sqrt{1/3}\|Z\downarrow\rangle-\sqrt{1/3}\|X-iY\uparrow\rangle$	$-E_A-\Delta_A$	$\|\frac{1}{2},-\frac{1}{2}\rangle$

TABLE II. Superlattice envelope-function equation [Eq. (4)] at $\mathbf{K}=(0,0,K_\perp)$ using modified Kane model as input. Only the positive M_J block is shown. The operator $\hat{\mathbf{k}}_z=-i(d/dz)$. The $\mathbf{K}=(0,0,K_\perp)$ superlattice energy is defined as $E_L(K_\perp)$.

$$\begin{bmatrix} V_{\Gamma_6}(z) & \frac{iP\hbar\hat{k}_z}{m} & 0 & \frac{iP\hbar\hat{k}_z}{\sqrt{2}m} \\ \frac{-iP\hbar\hat{k}_z}{m} & -E_A+V_{\Gamma_8}(z) & 0 & 0 \\ 0 & 0 & -E_A+V_{\Gamma_8}(z)-\frac{\hbar^2}{2}\hat{k}_z\frac{1}{m^{\mathrm{HH}}(z)}\hat{k}_z & 0 \\ \frac{-iP\hbar\hat{k}_z}{\sqrt{2}m} & 0 & 0 & -E_A-\Delta_A+V_{\Gamma_7}(z) \end{bmatrix} \begin{bmatrix} F_1(L,K_\perp;z) \\ F_3(L,K_\perp;z) \\ F_5(L,K_\perp;z) \\ F_7(L,K_\perp;z) \end{bmatrix} = E_L(K_\perp) \begin{bmatrix} F_1(L,K_\perp;z) \\ F_3(L,K_\perp;z) \\ F_5(L,K_\perp;z) \\ F_7(L,K_\perp;z) \end{bmatrix}$$

TABLE III. Superlattice quantities $A_n(z,E_L(K_\perp))$, $B_n(z,E_L(K_\perp))$, and $\bar{V}_n(z)$ which appear in the differential equations for the envelope functions [Eq. (5)].

n	1	2	3	4	5	6	7	8
$\lvert J,M_J\rangle$	$\lvert\frac{1}{2},+\frac{1}{2}\rangle$	$\lvert\frac{1}{2},-\frac{1}{2}\rangle$	$\lvert\frac{3}{2},+\frac{1}{2}\rangle$	$\lvert\frac{3}{2},-\frac{1}{2}\rangle$	$\lvert\frac{3}{2},+\frac{3}{2}\rangle$	$\lvert\frac{3}{2},-\frac{3}{2}\rangle$	$\lvert\frac{1}{2},+\frac{1}{2}\rangle$	$\lvert\frac{1}{2},-\frac{1}{2}\rangle$
$B_n(z,E_L(K_\perp))$	$\frac{\hbar^2P^2}{2m^2}\left[\frac{2}{E_L(K_\perp)+E_A-V_{\Gamma_8}(z)}+\frac{1}{E_L(K_\perp)+E_A+\Delta_A-V_{\Gamma_7}(z)}\right]$		$\frac{\hbar^2P^2}{m^2}\left[\frac{1}{E_L(K_\perp)-V_{\Gamma_6}(z)}\right]$		$-\frac{\hbar^2}{2}\frac{1}{m^{\mathrm{HH}}(z)}$		$\frac{\hbar^2P^2}{m^2}\left[\frac{1}{E_L(K_\perp)-V_{\Gamma_8}(z)}\right]$	
$A_n(z,E_L(K_\perp))$	1		$\frac{3E_L(K_\perp)+3E_A+2\Delta_A-2V_{\Gamma_7}(z)-V_{\Gamma_8}(z)}{2[E_L(K_\perp)+E_A+\Delta_A-V_{\Gamma_7}(z)]}$		1		$\frac{3E_L(K_\perp)+3E_A+2\Delta_A-2V_{\Gamma_7}(z)-V_{\Gamma_8}(z)}{2[E_L(K_\perp)+E_A-V_{\Gamma_8}(z)]}$	
$\bar{V}_n(z)$	$V_{\Gamma_6}(z)$		$V_{\Gamma_8}(z)-E_A$		$V_{\Gamma_8}(z)-E_A$		$V_{\Gamma_7}(z)-E_A-\Delta_A$	

$$\left[-\frac{d}{dz}B_n(z,E_L(K_\perp))\frac{d}{dz}A_n(z,E_L(K_\perp))+\bar{V}_n(z)\right]F_n(L,K_\perp;z)=E_L(K_\perp)F_n(L,K_\perp;z)\ . \tag{5}$$

The coefficients $A_n(z,E_L(K_\perp))$, $B_n(z,E_L(K_\perp))$, and $\bar{V}_n(z)$ are summarized in Table III for $n=1,\ldots,8$.[16] The specific forms of the envelope-function boundary conditions resulting from integration of Eq. (4) or Eq. (5) across an interface are obtained by requiring continuity of

$$B_n(z,E_L(K_\perp))\frac{d}{dz}A_n(z,E_L(K_\perp))F_n(L,K_\perp;z)$$

and

$$A_n(z,E_L(K_\perp))F_n(L,K_\perp;z)\ .$$

With these boundary conditions Eq. (5) can be solved analytically at $\mathbf{K}=\mathbf{0}$.

The $\mathbf{K}=\mathbf{0}$ SL states given by $\langle\mathbf{r}|L,0\rangle=\sum_n F_n(L,0;z)\langle\mathbf{r}|n0\rangle$ have either even ($P=+$) or odd ($P=-$) parity under $\mathbf{r}\to-\mathbf{r}$ within the present model. Therefore $\langle\mathbf{r}|L,0\rangle$ can be labeled by parity $P=\pm$ in addition to M_J. Table IV gives the analytic expressions for the nonvanishing $F_n(L,0;z)$'s corresponding to $\langle\mathbf{r}|L,0\rangle$'s with parity P and positive M_J in an A/B SL with layer widths l_A,l_B and period d.[17] Discontinuities in the envelope functions arise due to the truncated basis set.[6,14] The F_n's for the $-M_J$ SL states can be obtained from those of the $+M_J$ states by interchanging $F_1\leftrightarrow F_2$, $F_3\leftrightarrow F_4$, $F_5\leftrightarrow F_6$, and $F_7\leftrightarrow F_8$. The bulk $\mathbf{k}=\mathbf{0}$ Bloch functions $\langle\mathbf{r}|n0\rangle$ for $n=1$ and 2 transform like atomic s functions under operations of the tetrahedral group, while the $\langle\mathbf{r}|n0\rangle$'s for $n=3,\ldots,8$ transform like atomic p functions. Therefore for $\langle\mathbf{r}|L,0\rangle$'s with $P=+(-)$ the nonvanishing $F_n(L,0;z)$'s in Table IV are even (odd) for $n=1,2$ and odd (even) for $n=3,\ldots,8$, respectively. Analytic expressions for $E_L(0)$ appear in Ref. 5. The quantities k_A and k_B appearing in the expressions for the light particle (heavy-hole) SL states in Table IV, are bulk wave vectors for the bulk light particle (heavy-hole) bands at energy $E_L(0)$ in materials A and B, respectively.[5] Figure 1 indicates k_A and k_B for the case where L is a light particle SL band.

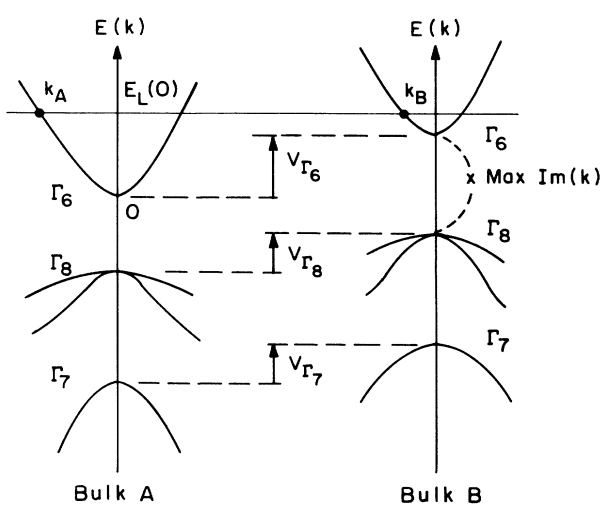

FIG. 1. Relative bulk band alignments of the Γ_6, Γ_7, and Γ_8 edges in materials A and B defining V_{Γ_6}, V_{Γ_7}, and V_{Γ_8}, respectively. The complex band structure associated with the bulk B band gap is shown dashed, and the maximum of the imaginary part of the bulk wave vector "Max Im(k)" is indicated. k_A (k_B) is the magnitude of the bulk wave vector along the growth axis at energy $E_L(0)$ in bulk material A (B).

The superlattice band structure $E_L(\mathbf{K})$ for $\mathbf{K}\neq\mathbf{0}$ can now be obtained using SL $\mathbf{K}\cdot\mathbf{p}$ theory. Writing

$$\langle\mathbf{r}|L,\mathbf{K}\rangle=\sum_{N'}c_{LN'}(\mathbf{K})e^{i\mathbf{K}\cdot\mathbf{r}}\langle\mathbf{r}|N'0\rangle \tag{6}$$

the SL $\mathbf{K}\cdot\mathbf{p}$ equation for SL band L at wave vector $\mathbf{K}$ becomes

$$\sum_N\left[\left[E_N(0)+\frac{\hbar^2K^2}{2m}-E_L(\mathbf{K})\right]\delta_{NN'}+\frac{\hbar\mathbf{K}}{m}\cdot\mathbf{P}_{NN'}\right]c_{LN'}(\mathbf{K})=0 \tag{7}$$

where $\mathbf{P}_{NN'}=\langle N0|\mathbf{p}|N'0\rangle$ is the SL momentum-matrix element at $\mathbf{K}=\mathbf{0}$. Equation (7) may be used to derive the f-sum rule, which yields the SL effective masses m_L for band L at $\mathbf{K}=\mathbf{0}$:

$$\left[\frac{m}{m_L}\right]_\alpha=1+\sum_{\substack{L'\\(L'\neq L)}}f^\alpha_{L'L}\ . \tag{8}$$

Here

$$f^\alpha_{L'L}=\frac{2}{m}\frac{|\langle L,0|p_\alpha|L',0\rangle|^2}{E_L(0)-E_{L'}(0)}\equiv\frac{(2/m)|P^\alpha_{LL'}|^2}{\Delta E_{LL'}(0)} \tag{9}$$

is the oscillator strength, $(2/m)|P^\alpha_{LL'}|^2=(2/m)|\langle L,0|p_\alpha|L',0\rangle|^2$ is an energy associated with the magnitude of the $\mathbf{K}=\mathbf{0}$ momentum-matrix element, and $\alpha=\perp(z)$ or $\parallel(x,y)$. The f-sum rule is also useful for discussing SL optical properties. The SL matrix elements appearing in Eqs. (7) and (8) are given by[1]

$$\langle L,0|p_{x(y)}|L',0\rangle=\sum_{nn'}\alpha_{nn'}(L,L')p^{x(y)}_{nn'}\ , \tag{10}$$

$$\langle L,0|p_z|L',0\rangle=\sum_{nn'}[\alpha_{nn'}(L,L')p^z_{nn'}+\Pi_n(L,L')\delta_{nn'}]\ , \tag{11}$$

where $\mathbf{p}_{nn'}=\langle n0|\mathbf{p}|n'0\rangle$ is the bulk momentum-matrix element, and

$$\alpha_{nn'}(L,L')=\frac{1}{d}\left[\int_{-l_{A/2}}^{l_{A/2}}+\int_{l_{A/2}}^{l_{A/2}+l_B}\right]dz\times F^*_n(L,0;z)F_{n'}(L',0;z)\ , \tag{12}$$

TABLE IV. Analytic solutions for the envelope function $F_n(L,0;z)$ in layer A (width l_A) and layer B (width l_B) corresponding to the superlattice $\mathbf{K}=\mathbf{0}$ states $|L,0\rangle_{M_J,P}$ which are labeled by the z component of angular momentum M_J and parity P. Only the $|L,0\rangle_{M_J,P}$ states with positive M_J are shown. For each $|L,0\rangle_{M_J,P}$ shown, only the nonvanishing F_n's are given. γ_A is defined to be $E_L(0)m/iP\hbar k_A$. N is the normalization constant. The bulk wave vectors k_A, k_B may be real or imaginary. The superlattice period $d=l_A+l_B$.

$\langle r\|L,0\rangle_{M_J,P}$		Im A: $-l_A/2<z<l_A/2$	Im B: $l_A/2<z<l_A/2+l_B$
$M_J=+\frac{1}{2}$	$F_1(L,0;z)$:	$N\cos k_A z$	$N\dfrac{\cos k_A l_A/2}{\cos k_B l_B/2}\cos k_B(z-d/2)$
$P=+$	$F_3(L,0;z)$:	$Ni\gamma_A\dfrac{2[E_A+\Delta_A+E_L(0)]}{3E_L(0)+3E_A+2\Delta_A}\sin k_A z$	$-Ni\gamma_A\dfrac{\sin k_A l_A/2}{\sin k_B l_B/2}\dfrac{2[E_A+\Delta_A+E_L(0)-V_{\Gamma_7}]}{3E_L(0)+3E_A+2\Delta_A-2V_{\Gamma_7}-V_{\Gamma_8}}\sin k_B(z-d/2)$
	$F_7(L,0;z)$:	$Ni\gamma_A\dfrac{\sqrt{2}[E_A+E_L(0)]}{3E_L(0)+3E_A+2\Delta_A}\sin k_A z$	$-Ni\gamma_A\dfrac{\sin k_A l_A/2}{\sin k_B l_B/2}\dfrac{\sqrt{2}[E_A+E_L(0)-V_{\Gamma_8}]}{3E_L(0)+3E_A+2\Delta_A-2V_{\Gamma_7}-V_{\Gamma_8}}\sin k_B(z-d/2)$
$M_J=+\frac{1}{2}$	$F_1(L,0;z)$:	$N\dfrac{i}{\gamma_A}\sin k_A z$	$-N\dfrac{i}{\gamma_A}\dfrac{\sin k_A l_A/2}{\sin k_B l_B/2}\sin k_B(z-d/2)$
$P=-$	$F_3(L,0;z)$:	$N\dfrac{2[E_A+\Delta_A+E_L(0)]}{3E_L(0)+3E_A+2\Delta_A}\cos k_A z$	$N\dfrac{\cos k_A l_A/2}{\cos k_B l_B/2}\dfrac{2[E_A+\Delta_A+E_L(0)-V_{\Gamma_7}]}{3E_L(0)+3E_A+2\Delta_A-2V_{\Gamma_7}-V_{\Gamma_8}}\cos k_B(z-d/2)$
	$F_7(L,0;z)$;	$N\dfrac{\sqrt{2}[E_A+E_L(0)]}{3E_L(0)+3E_A+2\Delta_A}\cos k_A z$	$N\dfrac{\cos k_A l_A/2}{\cos k_B l_B/2}\dfrac{\sqrt{2}[E_A+E_L(0)-V_{\Gamma_8}]}{3E_L(0)+3E_A+2\Delta_A-2V_{\Gamma_7}-V_{\Gamma_8}}\cos k_B(z-d/2)$
$M_J=+\frac{3}{2}$	$F_5(L,0;z)$:	$N\sin k_A z$	$-N\dfrac{\sin k_A l_A/2}{\sin k_B l_B/2}\sin k_B(z-d/2)$
$P=+$			
$M_J=+\frac{3}{2}$	$F_5(L,0;z)$;	$N\cos k_A z$	$N\dfrac{\cos k_A l_A/2}{\cos k_B l_B/2}\cos k_B(z-d/2)$
$P=-$			

$$\Pi_n(L,L')=\frac{1}{d}\left[\int_{-l_{A/2}}^{l_{A/2}}+\int_{l_{A/2}}^{l_{A/2}+l_B}\right]dz \times F_n^*(L,0;z)p_zF_n(L',0;z)\ . \quad (13)$$

The selection rules within the modified Kane model are $\langle L,0|p_{z(x)}|L',0\rangle=0$ unless (i) $M_J-M_{J'}=0(\pm1)$, *and* (ii) $|L,0\rangle$ and $|L',0\rangle$ have different parities.

For the SL's considered here, the $\alpha_{nn'}(L,L')p^z_{nn'}$ terms dominate over the $\Pi_n(L,L')$ terms in $\langle L,0|p_z|L',0\rangle$. Therefore the Kronig-Penney model is inadequate for calculating SL momentum-matrix elements since that model only contains Π terms. It can be shown[14,18] that for type-I SL's such as GaAs/$Ga_{1-x}Al_xAs$ having a gap much larger than the conduction- and valence-band offsets,

$$\langle L,0|p_z|L',0\rangle\sim(m/m_e^*)\Pi_n(L,L'),\quad n=1,2 \quad (14)$$

where $L=C1,C3,\ldots,$ $L'=C2,C4,\ldots,$ and m_e^* is the bulk electron mass. ($C1$ is the lowest SL conduction band.) The effect of $\Pi_n(L,L')$ in Eq. (11) is therefore smaller by about m/m_e^* than the first term. In the bulk limit (i.e., l_A or $l_B\rightarrow0$) the F_n's for $C2$ become sine or cosine waves with period d while the F_n's for $C1$ become constant. The α and Π integrals for $L=C1$ and $L'=C2$ vanish and $\langle C1,0|\mathbf{p}|C2,0\rangle$ is therefore zero. This behavior is consistent with that of a bulk intraband transition which vanishes in the absence of scattering. In a superlattice, the barrier layer supplies crystal momentum in the $\perp(z)$ direction. Hence $\langle C1,0|p_z|C2,0\rangle$ will be larger than $\langle C1,0|p_x|C2,0\rangle$.

III. ELECTRONIC PROPERTIES

The three types of superlattice (SL) being considered are shown in Fig. 2. The relative alignments of the Γ_6 and Γ_8 bulk band edges are shown for type-I (GaAs/$Ga_{1-x}Al_xAs$), type-II (InAs/GaSb), and type-III (HgTe/CdTe) A/B superlattices. Λ is the valence-band offset. Although the SL electron and hole states contain both Γ_6 *and* Γ_8 components, the solid line (Γ_6) can be associated roughly with the quantum well appropriate to electrons, and the dashed line (Γ_8) with that appropriate to holes. As indicated by the sketched envelope functions, the electron and hole in type-II SL's are therefore concentrated in layers A and B, respectively. By contrast both electron and hole are concentrated in layer A in type-I and -III SL's. The spectral limit theorem[19] implies that a positive SL gap always exists in type-I SL since there is a gap region common to both materials A and B. For type-II and -III SL's the gap may be zero.

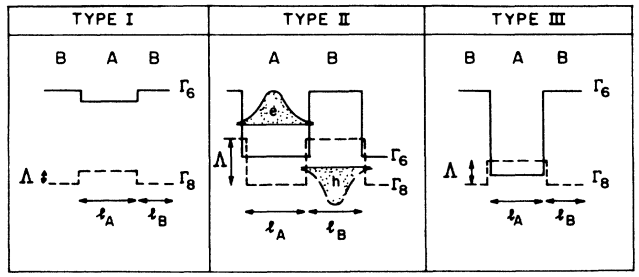

FIG. 2. Schematic band alignments for the three types of superlattice. The electron well associated with the Γ_6 conduction-band maximum (solid line) and the inverted hole well associated with the Γ_8 valence-band maximum (dashed line) are shown. The electron and hole envelope functions are shown schematically for a type-II superlattice, where the two are concentrated in adjacent layers. Λ is the valence-band offset.

Table V gives the bulk $\mathbf{k}\cdot\mathbf{p}$ parameters and valence-band offsets Λ used as input to the envelope-function equations [Eq. (5)]. Λ is taken as 350 meV for HgTe/CdTe (Ref. 3) in contrast to our previous zero offset analysis.[1] Although the qualitative features of Fig. 3 in Ref. 1 are unchanged, $m_\perp$ in the HgTe/CdTe SL is

TABLE V. Bulk $\mathbf{k}\cdot\mathbf{p}$ parameters and valence-band offsets (Λ) used as input to the superlattice envelope-function equations. $m_e^*(m_{HH}^*)$ is the bulk electron (heavy-hole) mass. $E(\Gamma_6)$, $E(\Gamma_7)$, and $E(\Gamma_8)$ are the energies of the Γ_6, Γ_7, and Γ_8 edges, respectively.

	Type I				Type II		Type III	
	GaAs (A)	$Ga_{0.7}Al_{0.3}As$[a] (B)	$In_{0.53}Ga_{0.47}As$ (A)	$In_{0.52}Al_{0.48}As$ (B)	InAs (A)	GaSb (B)	HgTe[b] (A)	CdTe[b] (B)
	$T=0$ K		$T=60$ K		$T=0$ K		$T=0$ K	
$E(\Gamma_6)-E(\Gamma_8)$ (eV)	1.52[c]	1.98	0.76[d]	1.47[d]	0.42[e]	0.81[e]	−0.30	1.60
$E(\Gamma_8)-E(\Gamma_7)$ (eV)	0.34[c]	0.32	0.35[a]	0.32[a]	0.38[e]	0.75[e]	1.0	0.90
Λ (eV)	0.138[f]		0.16[d]		0.57[e]		0.35	
m_e^*/m_0	0.067[g]	0.084	0.042[d]	0.075[d]	0.022	0.042[g]	0.031	0.11
m_{HH}^*/m_0	0.7[g]	0.7	0.5[a]	0.5[a]	0.4[e]	0.4[e]	0.7	0.7

[a]Virtual crystal alloy values.
[b]Reference 3.
[c]Reference 13.
[d]Reference 10.
[e]Reference 20.
[f]70:30 conduction-band:valence-band ratio (Ref. 21).
[g]Reference 22.

roughly twice as large for $\Lambda=350$ meV than for $\Lambda=0$ while $m_{\parallel}$ and E_g^{SL} both tend to be slightly smaller.

A. K=0 gaps and masses

Figure 3 shows the SL band gap E_g^{SL} and the $\mathbf{K}=0$ $C1$ electron masses $m_{\perp}$ (solid line), $m_{\parallel}$ (short-dashed line) as functions of layer width. The behavior can be understood qualitatively by considering the quantum well (QW) and homogeneous virtual crystal alloy (VCA) limits (dotted lines). The behavior of the effective masses will be discussed again in Sec. III B on the basis of the f-sum rule.

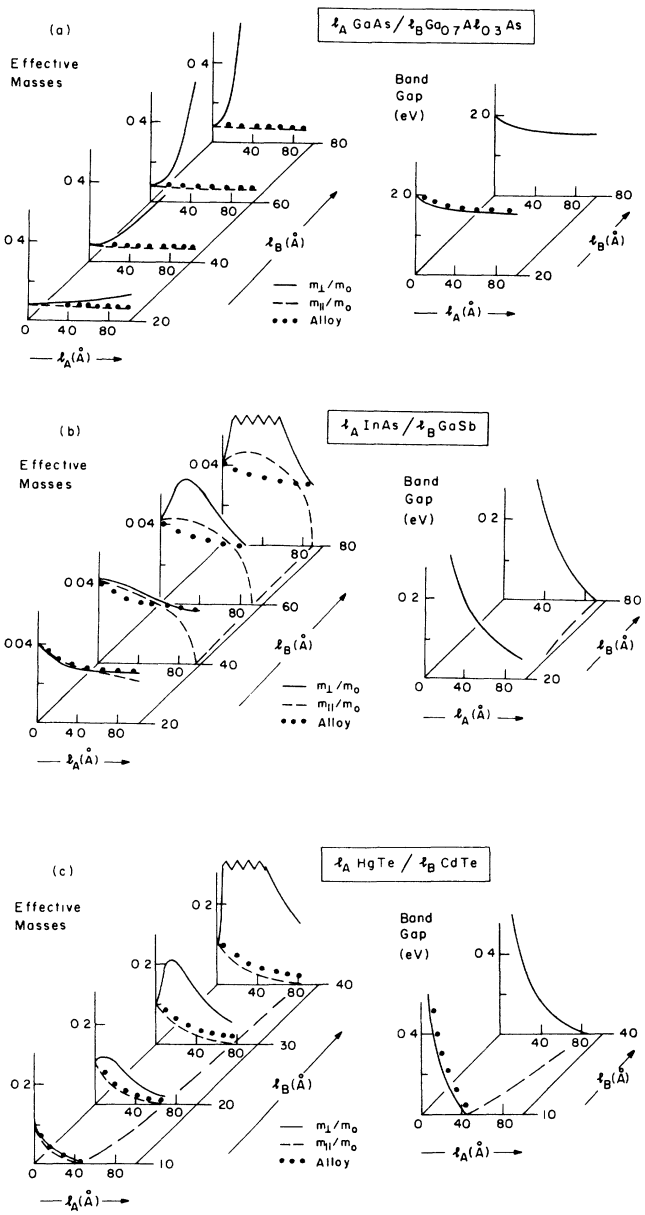

FIG. 3. Superlattice gap E_g^{SL} and the $\mathbf{K}=0$ $C1$ electron masses $m_{\perp}$ (solid line), $m_{\parallel}$ (short-dashed line) as functions of layer widths l_A, l_B in (a) $GaAs/Ga_{0.7}Al_{0.3}As$, (b) InAs/GaSb, and (c) HgTe/CdTe. The locus of $E_g^{SL}=0$ is indicated by a long-dashed line for InAs/GaSb and HgTe/CdTe. VCA masses and gaps for the alloy A_xB_{1-x} with $x=l_A/d$ are shown by dotted lines.

The QW picture is appropriate in the thick-barrier limit where $m_{\perp}$ is large. The SL band gap E_g^{SL} is then determined by the kinetic energies of confinement of the electrons and holes in their respective wells. In the QW picture, the energies of the electrons and holes are more sensitive to their respective well widths than the corresponding barrier widths. Furthermore, because of its lighter bulk mass, the electron confinement energy is more sensitive to the electron well width than the hole energy is to the model well width.

The VCA picture is appropriate in the thin-barrier SL limit where the envelope-function decay length in the barrier is much greater than the barrier thickness. In this limit the A/B SL is expected to behave like a homogeneous alloy A_xB_{1-x} where $x=l_A/d$ is the concentration of material A assumed to be uniformly dispersed throughout the sample. The VCA picture predicts that $m_{\parallel}$ and $m_{\perp}$ will be equal and follow E_g^{SL} as in the bulk.

For fixed barrier width l_B in each SL system, E_g^{SL} decreases as l_A increases, due to a reduction in the QW electron kinetic energy of confinement. In $GaAs/Ga_{1-x}Al_xAs$ [Fig. 3(a)] E_g^{SL} tends to the bulk GaAs gap with increasing l_A. Figure 2, on the other hand, suggests that in InAs/GaSb [Fig. 3(b)] and HgTe/CdTe [Fig. 3(c)] the gap E_g^{SL} becomes zero for large l_A because the decreasing electron confinement energy causes the electron energy level to fall below that of the hole level. In the VCA picture an increase in l_A is equivalent to an increase in x. Since the bulk A gap is less than that of bulk B, the VCA gap also decreases. The variation of the VCA gap for $GaAs/Ga_{1-x}Al_xAs$ and HgTe/CdTe using $x=l_A/d$ is shown by the dotted line in Fig. 3.[23] As expected the VCA gap agrees well with E_g^{SL} for thin barriers l_B.

In $GaAs/Ga_{1-x}Al_xAs$ and HgTe/CdTe, E_g^{SL} increases with increasing barrier thickness l_B at fixed l_A and saturates at the isolated quantum-well value. For InAs/GaSb the confinement energy of the electron increases as l_B becomes larger, but the hole confinement energy decreases. Hence E_g^{SL} may increase or decrease with increasing l_B depending on whether the electron or hole energy shift dominates.

Figure 3 shows that $m_{\parallel}$, indicated by the short-dashed line, decreases somewhat with increasing l_A in $GaAs/Ga_{1-x}Al_xAs$ and HgTe/CdTe for fixed l_B. This corresponds to the expected bulklike behavior for which $E_g^{SL}\sim m_{\parallel}$. In HgTe/CdTe $m_{\parallel}$ becomes zero for sufficiently large l_A as indicated by the long-dashed line in Fig. 3(c). As l_A is increased further, $m_{\parallel}$ actually becomes nonzero once more. A detailed account of the behavior of $m_{\parallel}$ and E_g^{SL} for HgTe/CdTe in this layer width regime is given in Ref. 3. The VCA masses, shown by a dotted line, agree well with $m_{\parallel}$ for thin barriers l_B. As shown in Fig. 3(b), $m_{\parallel}$ in InAs/GaSb exhibits a peak at $l_A\approx 25$ Å for GaSb widths greater than 40 Å. The corresponding electron energy level coincides with the max-

imum imaginary wave vector in the bulk GaSb gap [see the cross labeling "Max Im(k)" in Fig. 1]. The decay length of the electron wave function in GaSb is therefore a minimum, and the electron is maximally confined to the InAs layer. As a result the in-plane SL mass $m_{\parallel}$ resembles the bulk InAs electron mass $m^*_{\mathrm{InAs}}(E_{C1}(0))$ at a finite energy $E_{C1}(0)$ corresponding to the electron confinement energy above the InAs conduction-band edge. However the $l_A \rightarrow 0$ limit of $m_{\parallel}$ is given by the bulk GaSb electron mass $m^*_{\mathrm{GaSb}}(0)$, which is smaller than $m^*_{\mathrm{InAs}}(E_{C1}(0))$ due to the large conduction-band nonparabolicity in bulk InAs. This effect gives rise to a peak in $m_{\parallel}$.[24]

Turning now to the case where l_A is fixed and l_B is varying, we see that the behavior of $m_{\parallel}$ in all three SL systems is again similar to that of E_g^{SL} as described above.

Figure 3(a) shows that $m_{\perp}$ in GaAs/Ga_{1-x}AlAs increases with l_A at fixed l_B. The electron energy is lowered and as a result the effective barrier height is increased, and the tunneling probability is decreased. As indicated in Figs. 3(b) and 3(c) $m_{\perp}$ in InAs/GaSb and HgTe/CdTe exhibits a peak which occurs at the value of l_A for which the electron decay length in layer B is a minimum. The corresponding tunneling probability through layer B is therefore a minimum.[25]

Finally for fixed l_A, $m_{\perp}$ increases with increasing barrier thickness l_B in all the materials due to a decrease in tunneling probability.

B. f-sum rule

The behavior of $m_{\perp}$ and $m_{\parallel}$ of SL band $C1$ at $\mathbf{K}=\mathbf{0}$ can also be understood in terms of the f-sum rule, Eq. (8), with $f^{\alpha}_{L'L}$ given by Eq. (9). Type-I SL's have already been discussed in Ref. 1. We focus here on the somewhat more complicated type-II case, InAs/GaSb, for which the electron and hole envelope functions are confined in separate layers. Figure 4 shows the variation of $E_L(0)$, $(2/m)|P^{\alpha}_{L,C1}|^2$, and $f^{\alpha}_{L,C1}$ ($\alpha=\perp,\parallel$) for $L=C2$, $C1$, HH1, and LH1 (where HH denotes heavy hole and LH denotes light hole) as a function of well and barrier widths for InAs/GaSb. Three typical sets of layer widths (60 Å/40 Å, 40 Å/40 Å and 40 Å/60 Å) are considered to illustrate the behavior. The (40 Å InAs)/(40 Å GaSb) SL is used as a reference. The f-sum rule contributions to $C1$ from bands other than those given above are also listed, as are the values of $m_{\perp}$ and $m_{\parallel}$ obtained from Eq. (8). As shown by sketches for the (40 Å InAs)/(40 Å GaSb) SL, the $F_n(L,0;z)$'s are concentrated in InAs (layer A) for the electron states ($C1,C2$) and in GaSb (layer B) for the hole states (HH1, LH1). The Γ_8 (VB) edge of GaSb is taken to be the zero of energy.

We first focus on $C2$ and $C1$. The $C1 \rightarrow C2$ properties of InAs/GaSb are representative of those of type-I and type-III SL's. As indicated by the upward arrow in the $C2$ column, increasing l_A (the electron well width) from 40 to 60 Å at fixed $l_B=40$ Å causes $E_{C2}(0)$ to decrease from 0.67 to 0.42 eV, and $E_{C1}(0)$ to decrease from 0.16 to 0.052 eV due to a reduction in the electron confinement energy. Hence the energy difference $\Delta E_{C2,C1}(0)=E_{C2}(0)-E_{C1}(0)$ decreases. The energy $(2/m)|P^{\perp}_{C2,C1}|^2=(2/m)|\langle C2,0|p_{\perp}|C1,0\rangle|^2$ decreases from 4.9 to 4.5 eV as l_A increases since $(2/m)|P^{\perp}_{C2,C1}|^2$ vanishes in the bulk limit of pure A material. However,

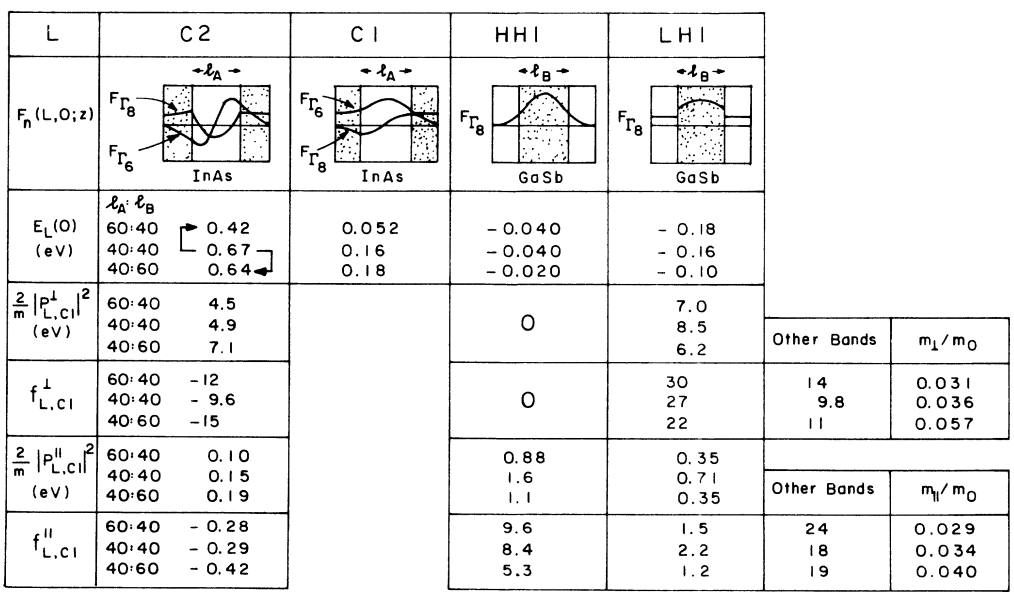

FIG. 4. Energies $E_L(0)$, $(2/m)|P^{\perp(\parallel)}_{L,C1}|^2=(2/m)|\langle L,0|p_{\perp(\parallel)}|C1,0\rangle|^2$, and oscillator strengths $f^{\perp(\parallel)}_{L,C1}$ for l_A InAs/l_B GaSb superlattice. Results are given for three sets of layer widths: 60 Å/40 Å, 40 Å/40 Å, and 40 Å/60 Å. The upward and downward arrows indicate increasing InAs (l_A) and GaSb (l_B) width, respectively. Dominant envelope functions are shown for the important $\mathbf{K}=\mathbf{0}$ superlattice states $L=C2$, $C1$, HH1, and LH1 in the (40 Å InAs)/(40 Å GaSb) superlattice. The total contribution from other superlattice bands is also listed. Superlattice masses are calculated using the f-sum rule Eq. (8).

$f^{\perp}_{C2,C1}$ increases in magnitude (from -9.6 to -12) because of the dominating variation of the energy denominator.

Along the same lines, as indicated by the downward arrow in the $C2$ column, increasing l_B (the electron barrier) from 40 to 60 Å at fixed $l_A = 40$ Å causes $\Delta E_{C2,C1}(0)$ to decrease. This change is small because the electron energies are insensitive to l_B for sufficiently thick barriers. The energy $(2/m)|P^{\perp}_{C2,C1}|^2$ increases from 4.9 to 7.1 as l_B increases because the deviation from bulk A behavior becomes larger. Alternatively, the increase in $(2/m)|P^{\perp}_{C2,C1}|^2$ can be viewed as resulting from the increased effectiveness of the barriers in supplying crystal momentum. The net result is an increase in the magnitude of $f^{\perp}_{C2,C1}$ from -9.6 to -15. The quantities $(2/m)|P^{\parallel}_{C2,C1}|^2$ and $f^{\parallel}_{C2,C1}$ are negligible since the parallel direction is essentially bulklike. We note in passing that a (40 Å GaAs)/(40 Å $Ga_{1-x}Al_xAs$) SL has a smaller energy $(2/m)|P^{\perp}_{C2,C1}|^2$ ($=1.5$ eV) associated with the $C1$-$C2$ matrix element[1] than (40 Å InAs)/(40 Å GaSb) because InAs, where the $C1 \rightarrow C2$ transition occurs, is far more nonparabolic than its GaAs counterpart.

There are several differences between the intersubband $C1 \rightarrow C2$ and valence–conduction-band $\mathrm{VB} \rightarrow C1$ properties (where VB≡HH1,LH1) of InAs/GaSb. In contrast to the electron energies $E_{C1}(0)$ and $E_{C2}(0)$, the hole energy $E_{\mathrm{VB}}(0)$ is more sensitive to l_B than l_A for large l_B, since the hole is located in the B layer. Furthermore, the energies $(2/m)|P^{\perp(\parallel)}_{\mathrm{VB},C1}|^2 = (2/m)|\langle \mathrm{VB},0|p_{\perp(\parallel)}|C1,0\rangle|^2$ are small compared to the bulk VB→CB value of 15 eV since the electron and hole are in adjacent layers. (Recall that $(2/m)|P^{\perp}_{C2,C1}|^2$ is smaller because of its intraband character.) The oscillator strength $f^{\perp(\parallel)}_{\mathrm{VB},C1}$ can however still be appreciable since $\Delta E_{C1,\mathrm{VB}}(0) = E_{C1}(0) - E_{\mathrm{VB}}(0)$ is also small. The quantity $f^{\perp}_{\mathrm{HH1},C1}$ vanishes because of the selection rules mentioned in Sec. II.

Unlike $(2/m)|P^{\perp}_{C2,C1}|^2$ which increases as l_B increases, the energies $(2/m)|P^{\perp(\parallel)}_{\mathrm{VB},C1}|^2$ decrease as either l_A or l_B is made larger. Specifically, for fixed $l_A = 40$ Å, increasing l_B from 40 to 60 Å causes both the electron and hole barriers to become more effective since the electron barrier thickness and the effective hole barrier height increase. As a result the electron-hole overlap is reduced. The decrease in $(2/m)|P^{\perp(\parallel)}_{\mathrm{VB},C1}|^2$ as l_A is increased for fixed $l_B = 40$ Å can be understood using a similar argument. In this case the hole barrier thickness and the effective electron barrier height increase.

In contrast to type-I SL's (Ref. 1) the values of $m_{\perp}$ shown in Fig. 4 are small and comparable to the VCA mass [see Fig. 3(b)] despite the fact that $f^{\perp}_{C2,C1}$ is large. Furthermore the contributions to the f-sum rule from HH1 and LH1 are small. The contributions from the excited hole states are therefore important as indicated in the column "Other Bands." For type-II SL, excited hole states near the top of the (Γ_8) hole well can leak into layer A thereby increasing the electron-hole overlap which leads to an appreciable contribution to the f-sum rule.

C. Finite K properties

The results for the SL energies and matrix elements at $\mathbf{K}=0$ can be used to obtain the band structure $E_L(\mathbf{K})$ for $\mathbf{K} \neq 0$ by diagonalizing the SL $\mathbf{K}\cdot\mathbf{p}$ matrix in Eq. (7). The SL matrix elements $\mathbf{P}_{LL'}(\mathbf{K}) = \langle L,\mathbf{K}|\mathbf{p}|L',\mathbf{K}\rangle$ for finite $\mathbf{K}$ are then calculated using the relationship $\mathbf{P}_{LL'}(\mathbf{K}) = \sum_{MM'} c^*_{LM}(\mathbf{K}) c_{L'M'}(\mathbf{K}) \langle M0|\mathbf{p}|M'0\rangle$, which follows from Eq. (6). The resulting SL properties are illustrated in Fig. 5 which shows $E_L(\mathbf{K})$ and $(2/m)|P^{\parallel}_{LL'}(\mathbf{K})|^2 = (2/m)|\langle L,\mathbf{K}|p_{\parallel}|L',\mathbf{K}\rangle|^2$ for (190 Å GaAs)/(200 Å $Ga_{0.75}Al_{0.25}As$), (37 Å InAs/37 Å GaSb), and (58 Å HgTe/42 Å $Hg_{0.15}Cd_{0.85}Te$) along the $K_{\parallel}$ and $K_{\perp}$ directions. Both $E_L(\mathbf{K})$ and $(2/m)|P^{\parallel}_{LL'}(\mathbf{K})|^2$ are independent of the direction of $\mathbf{K}_{\parallel}$ within the present model.

The valence-band structure calculated by Chang and Schulman[26] utilizing an elaborate tight-binding approach, which has been widely used, is shown by the dashed line for the GaAs/$Ga_{1-x}Al_xAs$ SL. The agreement with the present results is good for both the band structure and matrix elements even though only eight $|L,0\rangle$'s were explicitly included in the SL $\mathbf{K}\cdot\mathbf{p}$ matrix of Eq. (7), all other $|L,0\rangle$'s lying in the energy range from -2 to 2 eV being treated perturbatively. Sixteen $|L,0\rangle$'s were explicitly included in Eq. (7) in the cases of the InAs/GaSb and HgTe/$Hg_{1-x}Cd_xTe$ SL's in order to facilitate the calculation of optical properties, to be discussed in Sec. IV, over a wider energy range.

The $C1$ energy band for $K_{\perp}=0$, given by $E_{C1}(K_{\parallel})$, is reasonably parabolic in the $K_{\parallel}$ direction for each of the three SL's. However, the topmost valence bands show large nonparabolicity beyond π/d as a result of hybridization. The relative ordering of the LH1 and HH2 bands for each SL depends on the particular choice of SL layer widths. At $\mathbf{K}=0$ HH1 and LH1 are repelled strongly by $C1$ in the $K_{\parallel}$ direction. The repulsion between LH1 and HH2 is also appreciable since the bands are close in energy. LH1 therefore bends upward in the parallel direction for the InAs/GaSb SL due to the ordering of the LH1 and HH2 bands but bends down for the GaAs/$Ga_{1-x}Al_xAs$ and HgTe/$Hg_{1-x}Cd_xTe$ SL's. At finite $K_{\parallel}$ in the three SL's, the HH1 band contains a $|C1,0\rangle$ component to first order in the $\mathbf{K}\cdot\mathbf{p}$ interaction, and hence indirectly acquires a $|\mathrm{LH1},0\rangle$ component to second order in the $\mathbf{K}\cdot\mathbf{p}$ interaction. This leads to an anticrossing of HH1 and HH2 in the GaAs/$Ga_{1-x}Al_xAs$ SL and the HgTe/$Hg_{1-x}Cd_xTe$ SL at finite $K_{\parallel}$. In the InAs/GaSb SL the anticrossing involves LH1 and HH1. The HH3 band is flat in the parallel direction for the GaAs/$Ga_{1-x}Al_xAs$ SL since HH3 is not included in the more limited set used for this SL.

The energies $(2/m)|P^{\parallel}_{LL'}(\mathbf{K})|^2 = (2/m)|\langle L,\mathbf{K}|p_{\parallel}|L',\mathbf{K}\rangle|^2$ shown in Fig. 5 are relevant to the calculation of fundamental optical absorption discussed in Sec. IV, where the incident light propagates along the $z(\perp)$ axis and the polarization vector lies in the $xy(\parallel)$ plane. At $K_{\perp}=0$ the energies $(2/m)|P^{\parallel}_{LL'}(K_{\parallel})|^2$ depend sensitively on $K_{\parallel}$ due to the significant hybridization of the SL valence bands. In the GaAs/$Ga_{1-x}Al_xAs$ SL the crossing of LH1 and HH3 causes $(2/m)|P^{\parallel}_{C1,\mathrm{LH1}}(K_{\parallel})|^2$ to drop abruptly to zero at the LH1-HH3 crossing point. For larger $K_{\parallel}$ the now uppermost HH3 band does not interact with $C1$. The values of

$(2/m)|P^{\parallel}_{LL'}(\mathbf{K})|^2$ for the HgTe/$Hg_{1-x}Cd_xTe$ SL are seen to be smaller than those of the GaAs/$Ga_{1-x}Al_xAs$ SL. The state $|C1,0\rangle$ in the HgTe/$Hg_{1-x}Cd_xTe$ SL has an appreciable F_{Γ_8} component since the bulk HgTe conduction-band edge has Γ_8 symmetry, thereby reducing the matrix element between $C1$ and the SL valence bands. By contrast the InAs/GaSb matrix elements are small because the electron and hole are separated, as discussed in Sec. III B. In the HgTe/$Hg_{1-x}Cd_xTe$ SL the value of $(2/m)|P^{\parallel}_{C2,\mathrm{HH2}}(\mathbf{K})|^2$ is nearly equal to that of $(2/m)|P^{\parallel}_{C1,\mathrm{HH1}}(\mathbf{K})|^2$ because the envelope functions corresponding to $C2$ and HH2 both resemble first excited states in the same well.

The perpendicular band structure for $K_{\parallel}=0$, given by $E_L(K_{\perp})$, shows essentially no dispersion for the GaAs/$Ga_{1-x}Al_xAs$ SL since the $Ga_{1-x}Al_xAs$ layer is thick. The $K_{\parallel}=0$ energy $(2/m)|P^{\parallel}_{LL'}(K_{\perp})|^2$ shows a weak dependence on $K_{\perp}$ for GaAs/$Ga_{1-x}Al_xAs$ and HgTe/$Hg_{1-x}Cd_xTe$, in contrast to the InAs/GaSb SL. The stronger dependence in InAs/GaSb is associated with the electron and hole lying in different wells and has been discussed previously by Voisin *et al.*[27] In the InAs/GaSb SL, the interchange of $(2/m)|P^{\parallel}_{C1,\mathrm{LH1}}(K_{\perp})|^2$ and $(2/m)|P^{\parallel}_{C1,\mathrm{HH2}}(K_{\perp})|^2$ at finite $K_{\perp}$ is associated with the crossing of the LH1 and HH2 bands.

The preceding results all pertain to the valence-band offsets Λ listed in Table V. One of the remarkable properties of the HgTe/CdTe electronic structure is that a semiconductor $\rightarrow$semimetal$\rightarrow$ semiconductor transition occurs as the valence-band offset Λ (cf. Fig. 2) is increased from $\Lambda=0$. This behavior underlies our recently proposed resolution of the valence-band offset controversy in HgTe/CdTe SL's.[3] Explicitly it was shown in Ref. 3 that a large offset value ($\Lambda\approx350$ meV) is indeed consistent with the magneto-optical data of Berroir *et al.*[28] obtained from an unintentionally doped (100 Å HgTe)/(36 CdTe) SL sample. The experimental data had previously been interpreted as being uniquely associated with a small offset $\Lambda\approx40$ meV.

Figure 6 shows the band structure for the (100 Å HgTe)/(36 Å CdTe) SL for $\Lambda=40$, 230, and 350 meV. For small Λ (~40 meV) $C1$ lies above HH1 and the SL is semiconducting. As Λ is increased $C1$ drops in energy until it touches HH1 for $\Lambda=230$ mev, and the SL becomes semimetallic. For $\Lambda>295$ meV the SL is semiconducting once again as a result of the uncrossing of the $C1$ and HH1 bands. The band gap in this region is still direct but it occurs at the SL Brillouin-zone face $K_{\perp}=\pi/d$, as shown for $\Lambda=350$ meV.

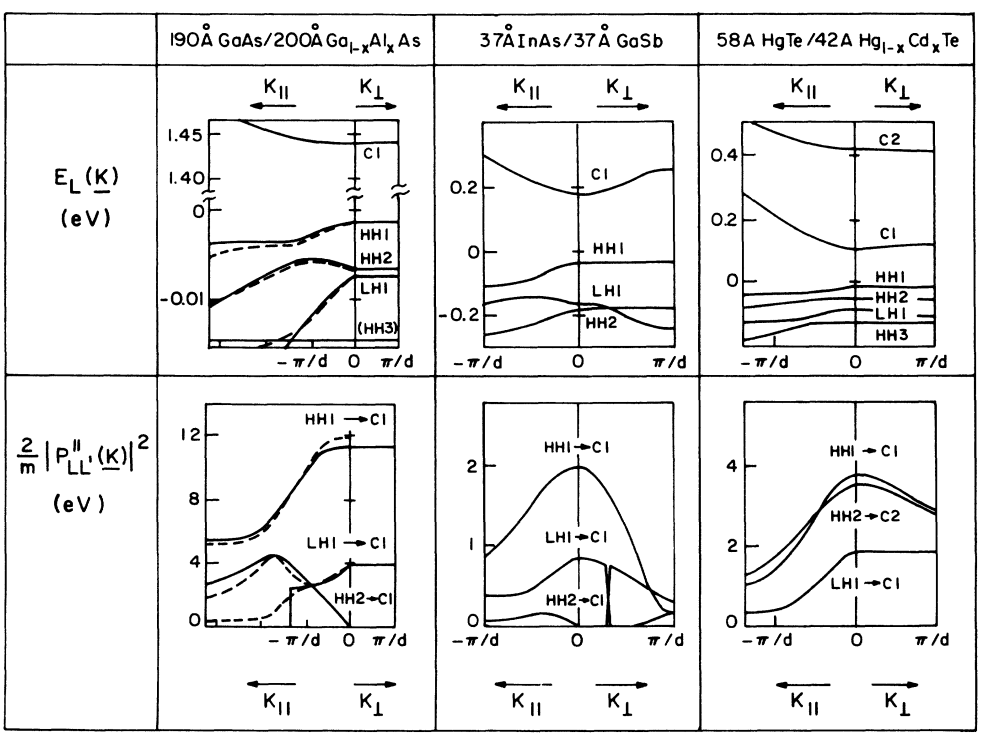

FIG. 5. Band structures $E_L(\mathbf{K})$ and energies $(2/m)|P^{\parallel}_{LL'}(\mathbf{K})|^2=(2/m)|\langle L,\mathbf{K}|p_{\parallel}|L',\mathbf{K}\rangle|^2$ for (190 Å GaAs)/(200 Å $Ga_{0.75}Al_{0.25}As$), (37 Å InAs)/(37 Å GaSb), and (58 Å HgTe)/(42 Å $Hg_{0.15}Cd_{0.85}Te$) superlattices shown as functions of $K_{\parallel}$ and $K_{\perp}$. The origin of energy is defined as the valence-band (Γ_8) edge of GaAs, GaSb, and HgTe, respectively. The label $L'\rightarrow L$ indicates the transition corresponding to $(2/m)|P^{\parallel}_{LL'}(\mathbf{K})|^2$. The superlattice growth axis is along the $\perp$ direction. The tight-binding results of Chang and Schulman (Ref. 26) are shown (dashed line) for comparison.

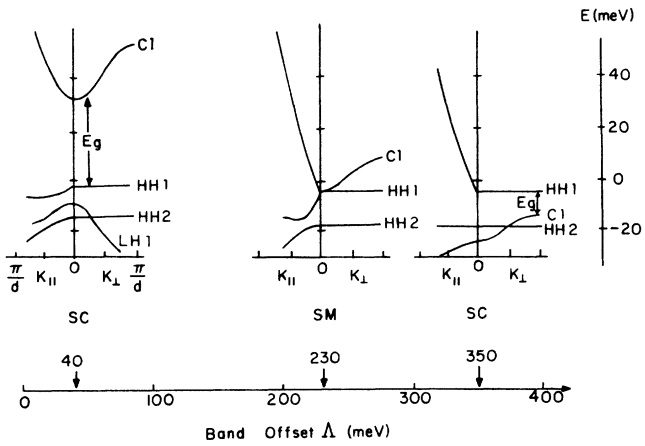

FIG. 6. The band structures for a (100 Å HgTe)/(36 Å CdTe) superlattice as a function of band offset Λ. As Λ increases, the system changes from semiconducting (SC) to semimetallic (SM) and back to semiconducting due to the crossing and uncrossing of the $C1$ and HH1 bands.

Figure 7 shows the nearly cylindrical constant energy surfaces of HH1 along $K_{\parallel}$ and $K_{\perp}$ for the (100 Å HgTe)/(36 Å CdTe) SL with $\Lambda=350$ meV. Energies are measured from the bottom of the HH1 band (0 meV). The bulges are a consequence of the $K_{\perp}$ dependence of the in-plane band structure. Assuming reasonable values of the intrinsic electron concentration ($n_c \geq 2\times10^{16}$ cm^{-3}) the calculated cyclotron mass is consistent with the zero field experimental value of 0.015±0.003. Recently, unintentional doping concentrations of $n_c \sim 5\times10^{15}$ cm^{-3} have been measured in other HgTe/CdTe samples.[29] Using $n_c=5\times10^{15}$ cm^{-3}, the calculated cyclotron mass becomes consistent with the experimental value for a band offset of $\Lambda \approx 370$ meV,[30] or possibly even a somewhat larger value.[31]

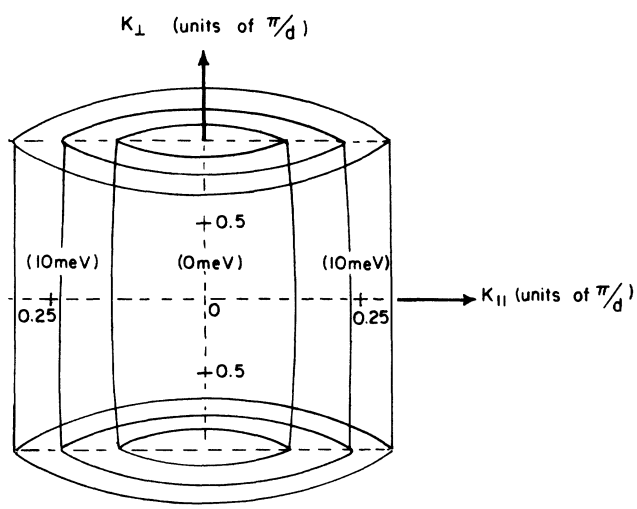

FIG. 7. Constant energy surfaces along $K_{\parallel}$ and $K_{\perp}$ of HH1 for a (100 Å HgTe)/(36 Å CdTe) superlattice with $\Lambda=350$ meV.

IV. OPTICAL PROPERTIES

The results of Sec. III C permit evaluation of the imaginary part of the dielectric function at frequency ω given by

$$\epsilon_2(\omega)=\frac{4\pi^2e^2}{\hbar m^2\omega^2}\sum_{LL'}\int\frac{d\mathbf{K}}{(2\pi)^3}|\langle L\mathbf{K}|\hat{\mathbf{e}}\cdot\mathbf{p}|L'\mathbf{K}\rangle|^2 \times\delta\left[\omega-\frac{E_{L'}(\mathbf{K})-E_L(\mathbf{K})}{\hbar}\right] \times[f(E_L(\mathbf{k}))-f(E_{L'}(\mathbf{K}))] =2n(\omega)\kappa(\omega) \quad (15)$$

where $L(L')$ is the SL band index of the initial (final) state, $\mathbf{K}$ is the SL wave vector and $f(E)$ is the Fermi-Dirac distribution. The unit vector $\hat{\mathbf{e}}$ defines the polarization of incoming light. The quantities $n(\omega)$ and $\kappa(\omega)$ are the real and imaginary parts of the refractive index.

The two optical processes of interest are fundamental absorption involving transitions between SL valence and conduction bands (Sec. IV A), and intersubband absorption involving transitions between the lowest two SL conduction bands $C1$ and $C2$ (Sec. IV B). Fundamental absorption in SL's is appreciable regardless of the polarization of the incident light, although for the cases of interest in Sec. IV A the polarization vector $\hat{\mathbf{e}}$ lies in the plane of the layers. Intersubband absorption is only appreciable if the polarization vector $\hat{\mathbf{e}}$ is perpendicular to the plane of the layers, and if there are carriers in $C1$.

The imaginary part of the dielectric function $\epsilon_2(\omega)=2n(\omega)\kappa(\omega)$ can be written as

$$\epsilon_2(\omega)=\epsilon_2^0(\omega)+\delta\epsilon_2^{C2,C1}(\omega)+\delta\epsilon_2^{CB,VB}(\omega) \quad (16)$$

where $\delta\epsilon_2^{C2,C1}(\omega)$ is associated with $C1\rightarrow C2$ absorption, $\delta\epsilon_2^{CB,VB}(\omega)$ is associated with fundamental absorption between SL valence (VB) and conduction (CB) bands within $\sim$0.5 eV of the onset, and $\epsilon_2^0(\omega)$ is the contribution associated with other occupied states. The real part of the dielectric function $\epsilon_1(\omega)\equiv n^2(\omega)-\kappa^2(\omega)$ is given by

$$\epsilon_1(\omega)=\epsilon_1^0(\omega)+\delta\epsilon_1^{C2,C1}(\omega)+\delta\epsilon_1^{CB,VB}(\omega) \quad (17)$$

where the individual contributions $\delta\epsilon_1^{C2,C1}(\omega)$, $\delta\epsilon_1^{CB,VB}(\omega)$, and $\epsilon_1^0(\omega)$ are obtained from $\delta\epsilon_2^{C2,C1}(\omega)$, $\delta\epsilon_2^{CB,VB}(\omega)$, and $\epsilon_2^0(\omega)$, respectively, using a Kramers-Kronig relation. The real part of the refractive index $n(\omega)$ is related to $\epsilon_1(\omega)$ and $\epsilon_2(\omega)$ by

$$n(\omega)=\left[\frac{\epsilon_1(\omega)}{2}+\tfrac{1}{2}[\epsilon_1^2(\omega)+\epsilon_2^2(\omega)]^{1/2}\right]^{1/2} \quad (18)$$

The absorption coefficient is defined as

$$\alpha(\omega)=\omega\epsilon_2(\omega)/n(\omega)c\ . \quad (19)$$

For light polarized perpendicular to the layers the $C1\rightarrow C2$ contribution to $\epsilon_2(\omega)$, given by $\delta\epsilon_2^{C2,C1}(\omega)$ in Eq. (16), is appreciable over a narrow energy range and at energies far below the onset of VB→CB transitions for the cases of interest. The corresponding contribution to $\epsilon_1(\omega)$, given by $\delta\epsilon_1^{C2,C1}(\omega)$ in Eq. (17), is a strong function

of ω in this frequency range and is equal to the principal part of $(2/\pi)\int_0^\infty d\omega'\omega'\delta\epsilon_2^{C2,C1}(\omega')/(\omega'^2-\omega^2)$. The frequency dependence of the refractive index $n(\omega)$ [Eq. (18)] must therefore be taken into account in calculating the intersubband absorption $\alpha(\omega)$ [Eq. (19)].

By contrast, the contribution $\epsilon_2^0(\omega)$ in Eq. (16) has a broad structure regardless of the polarization of incident light and only becomes appreciable at high energies (>2 eV). The corresponding contribution to $\epsilon_1(\omega)$, given by $\epsilon_1^0(\omega)$ in Eq. (17), is therefore reasonably independent of frequency ω over the energy range of interest $0<\hbar\omega<0.5$ eV. In addition $\epsilon_1^0(\omega)$ dominates $\delta\epsilon_1^{CB,VB}(\omega)$. For fundamental absorption with light polarized within the layer plane $\delta\epsilon_2^{C2,C1}(\omega)$ and $\delta\epsilon_1^{C2,C1}(\omega)$ are negligible; hence the refractive index $n(\omega)$ can be taken to be constant near the fundamental absorption edge. We have estimated the actual variation in $n(\omega)$ to be less than 10% using a two-band SL model.

A. Fundamental absorption

Figure 8 compares the experimental absorption curve (dashed line) for a (37 Å InAs)/(37 Å GaSb) SL at $T=4$ K (Ref. 8) with the present theoretical results (solid line). The agreement is seen to be satisfactory. The absorption coefficient $\alpha(E)$ is an order of magnitude smaller than that of a direct-gap bulk material because the electron and hole in the SL are concentrated in separate layers resulting in reduced overlap. The structure in $\alpha(E)$ mainly arises from the transitions HH1$\rightarrow C1$ and LH1$\rightarrow C1$ whose onsets are indicated by arrows. The corresponding partial contributions are indicated by long-dashed lines. The tail of the experimental absorption curve, which is not reproduced by the theory, is possibly due to disorder in the SL layer widths. The inset in Fig. 8 shows the modified theoretical absorption curve allowing for a randomly distributed ±4-Å fluctuation (corresponding to about a monolayer) in the individual layer widths, but keeping the SL period constant at 74 Å.

Figure 9 shows a similar comparison between the experimental[7] and theoretical absorption curves for a (58 Å HgTe)/(42 Å $Hg_{1-x}Cd_xTe$) SL at room temperature. The experimental results of Lansari *et al.*[7] (dashed line) are demonstrably reproducible in the sense that two separate samples grown under the same conditions yield an identical $\alpha(E)$ curve.[7] The experimental data show no evidence of a theoretically inexplicable tail, possibly indicating that the corresponding disorder in the InAs/GaSb sample is absent in the HgTe/$Hg_{1-x}Cd_xTe$ samples. The theoretical curve for $\Lambda=350$ meV (solid line) is in remarkable agreement with the experimental data. Although $\alpha(E)$ is not very sensitive to Λ the agreement between experiment and theory is better for $\Lambda=350$ meV than for $\Lambda=40$ meV (dashed-dotted line). The partial contributions for $\Lambda=350$ meV, shown by long-dashed lines, are again dominated by the HH1$\rightarrow C1$ and LH1$\rightarrow C1$ transitions at energies near the fundamental SL gap. The HH2$\rightarrow C2$ contribution near $E\sim0.5$ eV becomes comparable in magnitude to that of HH1$\rightarrow C1$ since the corresponding matrix elements are nearly equal (Sec. III C). The HH3$\rightarrow C3$ contribution is large for $E\sim0.8$ eV. Calculation of $\alpha(E)$ for $E>0.55$ eV is difficult since many SL bands contribute, and $E_L(\mathbf{K})$ is required for large $K_\parallel$ values. The HH3$\rightarrow C3$ contribution, shown by the dotted lines, was therefore included

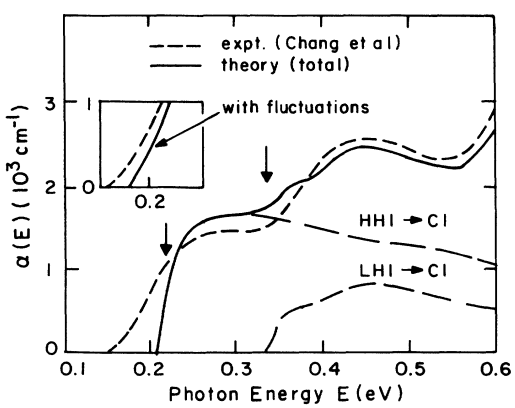

FIG. 8. Comparison of experimental coefficients (short-dashed line) of Chang *et al.* (Ref. 8) and theoretical (solid line) fundamental absorption coefficients $\alpha(E)$ as functions of photon energy E for (37 Å InAs)/(37 Å GaSb) at $T=4$ K. Dominant partial contributions are shown (long-dashed line). Inset: experimental vs theoretical tail of $\alpha(E)$ including a ±4-Å layer width fluctuation in the theory, at constant superlattice period.

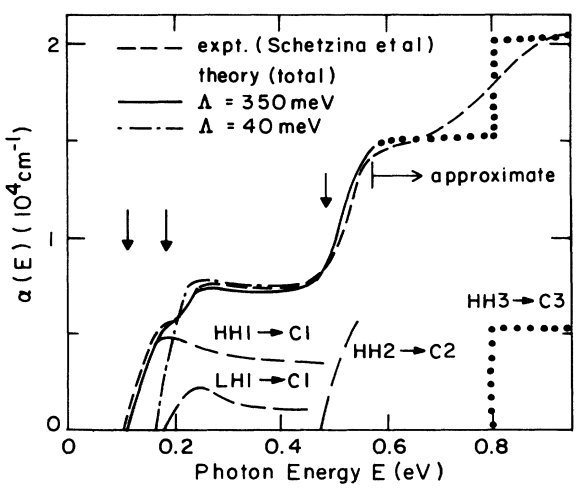

FIG. 9. Comparison of experimental coefficients (short-dashed line) of Lansari *et al.* (Ref. 7) and theoretical (solid line) fundamental absorption coefficients $\alpha(E)$ as a function of photon energy E for (58 Å HgTe)/(42 Å $Hg_{0.15}Cd_{0.85}Te$) at $T=300$ K. Λ is taken as 350 meV. Dominant partial contributions are shown (long-dashed line). Theoretical curve above $E=0.55$ eV is approximate (shown dotted). The theoretical absorption curve using $\Lambda=40$ meV is indicated by a dashed-dotted line.

approximately in Fig. 9 using a two-dimensional density of states and a **K**-independent SL matrix element. The observed structure in all cases, even the last, coincides with theoretically expected transitions.

The fundamental absorption in the $GaAs/Ga_{1-x}Al_xAs$ SL was not considered due to the importance of excitons which are not included in the present theory.

B. Intersubband absorption

In contrast to fundamental absorption, the $C1 \rightarrow C2$ absorption is only appreciable if the $C1$ band contains carriers, *and* the incident light is polarized perpendicular to the layers. The dependence of the $C1 \rightarrow C2$ absorption on the light polarization follows from the anisotropy of the $C1 \rightarrow C2$ oscillator strength $f^{\perp}_{C2,C1}$ discussed in Sec. III B (cf. Fig. 4). Several practical applications of the strong $C1 \rightarrow C2$ absorption have recently been suggested.

a. Carrier-activated light modulators. High-speed carrier-activated light modulation is possible in thick-barrier SL's (Ref. 2) where the $C1 \rightarrow C2$ absorption is large ($\sim 10^4$ cm^{-1}) and narrow (~ 10 meV) as a result of the large $C1 \rightarrow C2$ oscillator strength $f^{\perp}_{C2,C1}$ and the fact that the $C1$ and $C2$ bands are essentially parallel in all directions. The properties of $\alpha(E)$ and $n(E)$ will be illustrated here by considering an (80 Å GaAs)/(160 Å $Ga_{1-x}Al_xAs$) SL.

b. Infrared detectors. Levine *et al.*[12] have proposed an infrared detector consisting of $GaAs/Ga_{1-x}Al_xAs$ quantum wells with sufficiently thin well layers such that $C2$ lies in the continuum. The $C1 \rightarrow C2$ absorption of Ref. 12 is smaller and broader than for the case of Ref. 2 where both $C1$ and $C2$ are below the top of the well. As shown here, a thin-barrier SL also gives rise to a broad $\alpha(E)$ having a magnitude comparable to that of Ref. 12 ($\sim 10^3$ cm^{-1}). This is because the oscillator strength $f^{\perp}_{C2,C1}$ is small in the thin-barrier SL (Sec. III B) and the $C1$ and $C2$ bands have finite dispersions along the perpendicular direction. The specific thin layer SL system chosen here, (40 Å $In_xGa_{1-x}As$)/(20 Å $In_yAl_{1-y}As$) which corresponds to the bulk materials suggested by Levine *et al.*,[10] exhibits a larger high-energy cutoff for $\alpha(E)$ than a $GaAs/Ga_{1-x}Al_xAs$ SL of comparable layer widths. In the $GaAs/Ga_{1-x}Al_xAs$ SL, the $Ga_{1-x}Al_xAs$ X-point minimum imposes a lower wavelength limit of ~ 5 μm,[10] whereas in $In_xGa_{1-x}As/In_yAl_{1-y}As$ the limit is ~ 2 μm.

1. Thick-barrier limit

Equation (15) can be used to obtain a simple analytic form for $\delta\epsilon_2^{C2,C1}(\omega)$ for wide-gap SL's such as $GaAs/Ga_{1-x}Al_xAs$ in the thick-barrier limit. The $C1$ and $C2$ bands are dispersionless along the perpendicular direction. The in-plane dispersions of $C1$ and $C2$ are parabolic to a good approximation, with masses $m_{C1,\parallel}$ and $m_{C2,\parallel}$, respectively. In addition the matrix element $|\langle C1,\mathbf{K}|p_{\perp}|C2,\mathbf{K}\rangle|^2$ is essentially independent of **K** because the two bands are nearly parallel.

At $T=0$ K the expression for $\delta\epsilon_2^{C2,C1}(\omega)$ reduces to

$$\delta\epsilon_2^{C2,C1}(\omega)=\begin{cases}\dfrac{4\pi^2e^2}{m^2\omega^2}\left[\dfrac{m_{r,\parallel}}{\pi\hbar^2 d}\right]|\langle C1,0|p_{\perp}|C2,0\rangle|^2 & \text{if } E_g^{C2,C1}(0)>\hbar\omega>E_g^{C2,C1}(K_{\parallel}=K_F)\\ 0 & \text{otherwise}\end{cases} \tag{20}$$

where $(m_{r,\parallel}/\pi\hbar^2 d)$ is the $C1 \rightarrow C2$ joint density of states with $m_{r,\parallel}/m=(m/m_{C1,\parallel}-m/m_{C2,\parallel})^{-1}$. The in-plane masses $m_{C1,\parallel}$ and $m_{C2,\parallel}$ differ slightly because of nonparabolic band effects in the bulk. The low-energy cutoff for $\delta\epsilon_2^{C2,C1}(\omega)$ is $E_g^{C2,C1}(K_{\parallel}-K_F)$ where $E_g^{C2,C1}(K_{\parallel})=E_{C2}(K_{\parallel})-E_{C1}(K_{\parallel})$ and K_F is the Fermi wave vector along the parallel direction. It follows that the absorption width $E_g^{C2,C1}(0)-E_g^{C2,C1}(K_{\parallel}=K_F)$ is $\pi n_{C1}\hbar^2 d/m_{r,\parallel}$ where n_{C1} is the concentration of electrons in $C1$ and $n_{C2}=0$.

Since $C1$ and $C2$ are essentially parallel, $m_{r,\parallel}$ is large, and therefore $\delta\epsilon_2^{C2,C1}(\omega)$ is large and narrow. Figure 10 shows the corresponding $\alpha(E)$ (dashed line) and $n(E)$ (solid line) for (80 Å GaAs)/(160 Å $Ga_{0.7}Al_{0.3}As$) at $T=300$ K with $n_{C1}=5\times10^{17}$ cm^{-3}. The 5-meV width is comparable to a laser linewidth. The sharp structure in $\alpha(E)$ is accompanied by a large variation in the refractive index $n(E)$. The sensitivity of $n(E)$ to the photon energy E has potential application in high-speed light modulation.[2] The slight smearing on the low-energy side of $\alpha(E)$ is due to the finite temperature Fermi distribution.

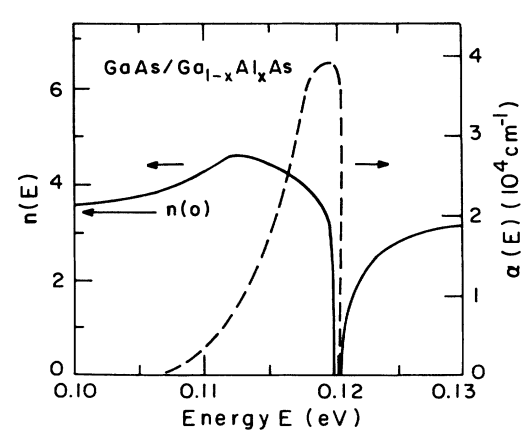

FIG. 10. Calculated refractive index $n(E)$ (solid line; left-hand scale) and absorption coefficient $\alpha(E)$ (dashed line; right hand scale) vs photon energy E for (80 Å GaAs)/(160 Å $Ga_{0.7}Al_{0.3}As$) at $T=300$ K, for $C1$ electron concentration $n_{C1}=5\times10^{17}$ cm^{-3}. The incident light is polarized perpendicular to the layers.

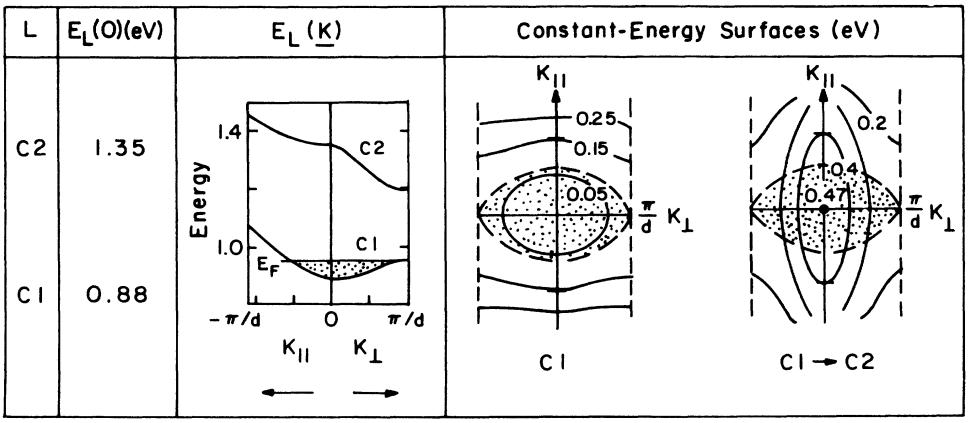

FIG. 11. $C1$ and $C2$ band structure for (40 Å $In_{0.53}Ga_{0.47}As$)/(20 Å $In_{0.52}Al_{0.48}As$), together with $C1$ constant energy surfaces and $C1 \rightarrow C2$ constant energy surfaces. The chemical potential $E_F(T=60\ \mathrm{K})=0.065$ eV corresponds to a $C1$ electron concentration of $n_{C1}=1.4\times10^{18}\ \mathrm{cm}^{-3}$. The shaded region of **K** space corresponds to **K** points at which the probability of occupation of $C1$ is greater than $\frac{1}{2}$.

The results plotted in Fig. 10 obey the sum rule

$$\int_0^\infty \omega\delta\epsilon_2^{C2,C1}(\omega)d\omega \approx \frac{2n_c\pi^2e^2}{m_e^*} = \frac{\pi}{2}\omega_p^2 , \qquad (21)$$

where n_c is the electron density, m_e^* is the bulk electron mass ($m_e^* \sim 0.07m$), and the plasma frequency $\omega_p^2 = 4\pi n_c e^2/m_e^*$, to a good approximation. This will not be the case for the thin-barrier SL to be discussed later. The magnitude of the absorption curve in the thick-barrier SL, which is larger than that for the interband bulk absorption, is a consequence of its narrow energy range. Substituting the general expression for $\delta\epsilon_2^{C2,C1}(\omega)$ in a thick-barrier SL [Eq. (20)] into Eq. (21) yields $|f_{C2,C1}^{\perp}| \simeq m/m_e^*$. This approximate result for $|f_{C2,C1}^{\perp}|$ is verified for the (80 Å GaAs)/(160 Å $Ga_{1-x}Al_xAs$) SL in Fig. 10 where $|f_{C2,C1}^{\perp}| = 13.5$ compared to $m/m_e^* = 15$.

Physically, the magnitude of $\alpha(E)$ in Fig. 10 can be understood using a bulk free carrier absorption model for the $C1 \rightarrow C2$ transition. Explicitly, the barrier (B) atoms are imagined to be homogeneously distributed throughout the SL sample giving rise to scattering of the electrons. The impurity concentration of B atoms required for a bulk free carrier absorption of magnitude $\sim 10^4\ \mathrm{cm}^{-1}$ roughly corresponds to the concentration of barrier atoms within the spatial extent of the $C1$ envelope function in the barrier (~ 30 Å).

2. *Thin-barrier limit*

Figure 11 shows the $C1$ and $C2$ band structure for (40 Å $In_{0.53}Ga_{0.47}As$)/(20 Å $In_{0.52}Al_{0.48}As$) together with the $C1$ constant energy surfaces, and the $C1 \rightarrow C2$ constant energy surfaces. The nonzero dispersion of $C1$ and $C2$ along the perpendicular direction gives reduced nesting between the $C1$ and $C2$ bands compared to the thick-barrier case. The energy difference $E_{C2}(\mathbf{K}) - E_{C1}(\mathbf{K})$ is a maximum at $\mathbf{K}=\mathbf{0}$ which represents a high-energy cutoff of 0.47 eV (2.6 μm) for the $C1 \rightarrow C2$ transition. The $\mathbf{K}=\mathbf{0}$ oscillator strength $f_{C2,C1}^{\perp}$ is -4.0 and therefore smaller than the thick-barrier GaAs/$Ga_{1-x}Al_xAs$ value of -13.5. We consider the situation with carriers in $C1$ at temperature T, and a Fermi level at energy $E_F(T)$ above the $C1$ edge. The shaded portions in Fig. 11 correspond to the region in **K** space where the $C1$ band is occupied for an electron concentration $n_{C1}=1.4\times10^{18}$ cm^{-3} at $T=60$ K [$E_F(T)=0.065$ eV]. The $C2$ band is empty, hence $C1 \rightarrow C2$ transitions will occur at wave vectors **K** within this shaded region. As seen from the $C1 \rightarrow C2$ constant energy surfaces in Fig. 11, the number of $C1 \rightarrow C2$ transitions occurring at a given incident photon energy E is a weak function of E over the range

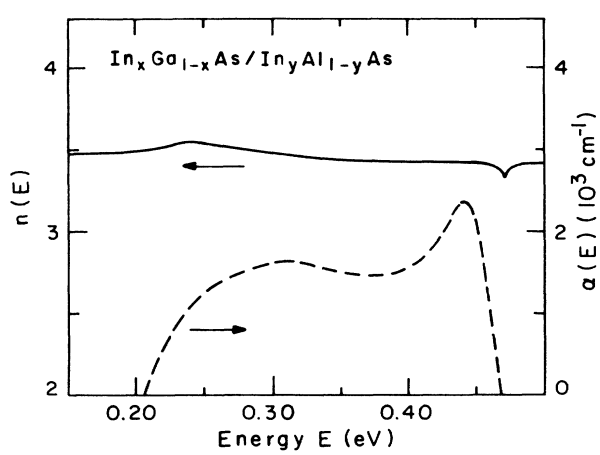

FIG. 12. Calculated refractive index $n(E)$ (solid line; left-hand scale) and absorption coefficient $\alpha(E)$ (dashed line; right-hand scale) vs photon energy E for (40 Å $In_{0.53}Ga_{0.47}As$)/(20 Å $In_{0.52}Al_{0.48}As$) at $T=60$ K, for $C1$ electron concentration $n_{C1}=1.4\times10^{18}\ \mathrm{cm}^{-3}$. The incident light is polarized perpendicular to the layers.

$0.25 < E < 0.45$ eV, therefore the absorption curve will be reasonably flat. Figure 12 shows the corresponding $\alpha(E)$ (dashed line) and $n(E)$ (solid line) for (40 Å $In_xGa_{1-x}As$)/(20 Å $In_yAl_{1-y}As$). The broad structure in $\alpha(E)$ yields a weaker variation in $n(E)$ than for the thick-barrier SL. The small peak in $\alpha(E)$ near 0.45 eV is reminiscent of a one-dimensional joint density of states and is associated with the near parallelism of $C1$ and $C2$ in the two in-plane ($K_{\parallel}$) directions.

In the thin-barrier limit considered in Fig. 12 the ϵ_2-sum rule of Eq. (21) is only approximately half exhausted by the $C1 \rightarrow C2$ transition as a result of the finite band dispersion along the perpendicular direction. This effect causes nonzero free carrier absorption within $C1$ and also gives greater relative weight to transitions to higher minibands. The ϵ_2-sum rule therefore provides an upper bound to the $C1 \rightarrow C2$ absorption strength in the thin-barrier SL. The important consequence of the sum rule is that a narrow, large $C1 \rightarrow C2$ absorption in thick-barrier SL's becomes not only broader, but also considerably smaller for thin-barrier SL's than would be the case if the $C1 \rightarrow C2$ transition still exhausted the sum rule.

ACKNOWLEDGMENTS

This work was supported by the U.S. Defense Advanced Research Agency (DARPA) through U.S. Office of Naval Research (ONR) Contract No. N00014-86-K-0033 and by the U.S. Joint Service Electronics Program (JSEP) through ONR Contract Nos. N00014-84-K-0465 and N00014-89-J-1023. One of us (P.M.Y.) would like to acknowledge the Fannie and John Hertz Foundation for partial financial support.

---

*To whom all correspondence should be addressed.

[1]N. F. Johnson, H. Ehrenreich, K. C. Hass, and T. C. McGill, Phys. Rev. Lett. **59**, 2352 (1987).

[2]N. F. Johnson, H. Ehrenreich, and R. V. Jones, Appl. Phys. Lett. **53**, 180 (1988).

[3]N. F. Johnson, P. M. Hui, and H. Ehrenreich, Phys. Rev. Lett. **61**, 1993 (1988); P. M. Hui, H. Ehrenreich, and N. F. Johnson, J. Vac. Sci. Technol. A **7**, 424 (1989).

[4]M. Altarelli, Phys. Rev. B **28**, 842 (1983).

[5]G. Bastard, in *Proceedings of the NATO Advanced Study Institute on Molecular Beam Epitaxy in Heterostructures, Erice, Italy, 1983,* edited by L. L. Chang and K. Ploog (Martinus-Nijhoff, Dordrecht, 1984), p. 381.

[6]N. F. Johnson, H. Ehrenreich, G. Y. Wu, and T. C. McGill, Phys. Rev. B **38**, 13 095 (1988).

[7]Y. Lansari, J. W. Hans, S. Hwang, L. S. Kim, J. W. Cook, Jr., and J. F. Schetzina, J. Vac. Sci. Technol. A **7**, 241 (1989).

[8]L. L. Chang, G. A. Sai-Halasz, L. Esaki, and R. L. Aggarwal, J. Vac. Sci. Technol. **19**, 589 (1981).

[9]L. C. West and S. J. Eglash, Appl. Phys. Lett. **46**, 1156 (1985).

[10]B. F. Levine, K. K. Choi, C. G. Bethea, J. Walker, and R. J. Malik, Appl. Phys. Lett. **52**, 1481 (1988).

[11]P. Yuh and K. L. Wang, Appl. Phys. Lett. **51**, 1404 (1987).

[12]B. F. Levine, C. G. Bethea, K. K. Choi, J. Walker, and R. J. Malik, J. Appl. Phys. **64**, 1591 (1988).

[13]E. O. Kane, in *Narrow Gap Semiconductors: Physics and Applications,* Vol. 133 of *Lecture Notes in Physics,* edited by W. Zawadski (Springer-Verlag, New York, 1981), p. 13.

[14]N. F. Johnson, Ph.D. thesis, Harvard University, 1989.

[15]Inclusion of finite spin-orbit splitting, Δ, is necessary for an accurate description of excited SL hole states with energies comparable to Δ.

[16]In fact Eq. (5) holds for a general heterostructure state at $\mathbf{K}_{\parallel}=\mathbf{0}$, if the SL labels L and $K_{\perp}$ are dropped.

[17]The expressions for the F_n's reduce to those of M. de Dias Leyva and J. Lopez Gondar, Phys. Status Solidi B **128**, 575 (1985) in the limit of infinite spin-orbit splitting.

[18]The derivation of Eq. (14) is similar to the bulk impurity problem considered by W. Kohn, in *Solid State Physics,* edited by F. Seitz and D. Turnbull (Academic, New York, 1967), Vol. 5, p. 284.

[19]H. Ehrenreich and L. Schwartz, in *Solid State Physics,* edited by H. Ehrenreich, F. Seitz, and D. Turnbull (Academic, New York, 1976), Vol. 31, p. 149.

[20]G. Bastard, Acta Electron. **25**, 147 (1983).

[21]See, for example, J. Menendez, A. Pinczuk, D. J. Werder, A. C. Gossard, and J. H. English, Phys. Rev. B **33**, 8863 (1986).

[22]D. Long, *Energy Bands in Semiconductors* (Wiley, New York, 1968), p. 195.

[23]For an InAs/GaSb SL (type II), the electron and hole do not have common barriers. Therefore *both* layers must be thin before the VCA gap ($x = l_A/d$) will adequately describe the actual SL gap in InAs/GaSb. The VCA gap lies above the energy scale shown in Fig. 3(b) for the ranges of SL layer widths considered.

[24]The HgTe/CdTe SL does not exhibit a distinguishable peak in $m_{\parallel}$ as a function of HgTe width l_A since the bulk CdTe mass m^*_{CdTe}, which represents the $l_A \rightarrow 0$ limit of $m_{\parallel}$, is large ($m^*_{\mathrm{CdTe}} = 0.11 m_0$).

[25]The peaks in $m_{\perp}$ and $m_{\parallel}$ for InAs/GaSb both occur near $l_A = 25$ Å.

[26]Y. C. Chang and J. N. Schulman, Phys. Rev. B **31**, 2069 (1985).

[27]P. Voisin, G. Bastard, and M. Voos, Phys. Rev. B **29**, 935 (1984).

[28]J. M. Berroir, Y. Guldner, J. P. Vieren, M. Voos, and J. P. Faurie, Phys. Rev. B **34**, 891 (1986).

[29]M. Voos (private communication).

[30]P. Young, H. Ehrenreich, and N. F. Johnson (unpublished).

[31]Further evidence for a large band offset has recently been provided by M. Voos, J. Manasses, J. M. Berroir, Y. Guldner, J. P. Vieren, X. Chu, and J. P. Faurie, in Proceedings of the 4th International Conference on Modulated Semiconductor Structures, Ann Arbor, 1989 (Surf. Sci., to be published).